Applied Acoustics 220 (2024) 109965

Contents lists available at ScienceDirect

Applied Acoustics

journal homepage: www.elsevier.com/locate/apacoust

Metasurfaces for sound absorption over a broad range of wave incidence angles

Diana Maria Garza-Agudelo [a,b,*], Vicente Cutanda Henriquez [c], Cheol-Ho Jeong [a], Peter Risby Andersen [d], Martin Ibarias [e], José Sanchez-Dehesa [e], Frieder Lucklum [c]

[a] Acoustic Technology, Department of Electrical and Photonics Engineering, Technical University of Denmark, Ørsteds Plads, Building 352, Kongens Lyngby, 2800, Denmark
[b] Oticon A/S, Kongebakken 9, Smørum, 2765, Denmark
[c] Center for Acoustic-Mechanical Microsystems, Department of Electrical and Photonics Engineering, Technical University of Denmark, Ørsteds Plads, Building 352, Kongens Lyngby, 2800, Denmark
[d] Audio Research GN Audio A/S & Jabra, Lautrupbjerg 7, Ballerup, 2750, Denmark
[e] Department of Electronic Engineering, Universitat Politècnica de València, Camino de Vera s.n., Building 7F, Valencia, ES-46022, Spain

ARTICLE INFO

Keywords:
Acoustic absorption
Oblique absorption
Acoustic metamaterial
Absorbing metasurface
Sonic crystal

ABSTRACT

Control of reflected waves that meet surfaces from oblique directions is crucial, for instance, in closed spaces. Metasurfaces composed of Helmholtz resonators can be efficient and compact absorbers but have limited ability to achieve high absorption over a wide incidence angle range, especially when designed for high performance in the region approaching grazing incidence. In turn, sonic crystals can be used to manipulate wave propagation direction at low frequencies. We propose a type of absorber that combines a surface of 2D Helmholtz resonators and a 2D sonic crystal with cylindrical scatterers arranged in a hexagonal lattice. The combined effect of both structures yields a metasurface that can achieve high absorption over a broad range of incidence angles. Here, an analytic model to estimate the behavior of the absorbers for wavelengths that are much longer than the unit cell dimensions is presented. The model is used in combination with an optimization strategy to realize designs for single frequency and octave-band performance. The test cases show that surfaces with absorption coefficient values above 0.9 for the range of incidence angle extending from 0° until 83° can be realized. The performance of the absorbers is verified with a finite element model and experimentally.

1. Introduction

Acoustic absorbing materials are used in a wide variety of engineering applications such as acoustic reflections control, reverberation time adjustment, noise control in closed spaces, as integral parts of sound barriers, and more [1]. In closed spaces, there is often a large number of sound sources and/or reflective elements which yield sound fields that are composed of waves traveling in many directions. When effective reflection control is desired, surface materials that provide high absorption over a broad range of incidence angles are preferable. As an example, in spaces like disproportionate rooms, the range of angles at which first-order reflections take place can extend to near-grazing incidence [2]. In this paper, we propose a type of acoustic metasurface (AM) that can achieve high absorption over a large range of wave incidence angles. It consists of a 2D sonic crystal with cylindrical scatterers arranged in a hexagonal lattice which is placed over a periodic surface of parallel 2D Helmholtz resonators. It is designed for high absorption in the frequency range where wavelengths are much longer than the dimensions of the structure.

In recent years, the potential of sound absorbing metasurfaces as compact alternatives to traditional porous absorbers has been highlighted [3]. Often, these metasurfaces are realized as periodic arrangements of Helmholtz or quarter wavelength resonators. By designing unit cells that combine nonidentical resonators, the operational frequency range of these AM can be extended [4–7]. Nevertheless, arrangements of resonators have a behavior that can be approximated as locally reacting, and thus their ability to achieve high absorption over an extended range of angles is limited [8–10]. This is especially critical when they

* Corresponding author.
E-mail address: dimg@demant.com (D.M. Garza-Agudelo).

https://doi.org/10.1016/j.apacoust.2024.109965
Received 21 October 2023; Received in revised form 4 February 2024; Accepted 5 March 2024
Available online 18 March 2024

are designed for maximum absorption in the region near grazing incidence given the high rate of variation of the radiation impedance with the incidence angle [9].

Additionally, previous works have shown that structured arrangements of cylinders can be used to influence wave propagation at frequencies with wavelengths that are much longer than the spacing between elements. For instance, arrangements of this type have been proposed to achieve sound focusing [11,12], acoustic cloaking [13], and acoustic absorption [14–17]. Within the works related to sound absorption, Guild et al. studied the behavior of two-dimensional sonic crystals as absorbing materials [14], and Elliot et al. [15], Climente et al. [16] and Cutanda Henríquez and Sánchez-Dehesa [17] studied engineered structures of cylinders as part of acoustic black holes. In the latter application, the arrangements of cylinders have been used to realize gradient-index lenses that guide the propagating wave towards the absorbing core of the black hole [15,16], or to realize the absorbing core [16,17].

In the AM proposed here, the Helmholtz resonators act as efficient subwavelength absorbers, whilst the sonic crystal is used to modify the wave propagation above the resonators in order to extend the range of incidence angles for which high absorption is achieved. We introduce analytic and numerical models to estimate the sound absorption coefficient of the proposed AMs, and an efficient gradient-based optimization strategy to design metasurfaces that achieve broad angular absorption at a predefined frequency range. Specific examples of surfaces for single and multifrequency performance are demonstrated and discussed. To the best of the authors' knowledge, compact absorbing surfaces designed explicitly for wide multidirectional performance have only been proposed by Cavalieri et al. [18] using anisotropic porous materials. Moreover, a surface combining an arrangement of resonators with a two-dimensional sonic crystal has not been proposed previously in the literature.

The remaining of this document is organized as follows: in Section 2, background theory and details of the analytic and numerical models used to estimate the absorbing behavior of the AMs under consideration are presented. In Section 3, the design procedure based on parameter optimization of the surfaces geometry is presented. In Section 4, specific designs of AMs with broad angle range of high absorption for a single and a multifrequency case are presented. The behavior of the surface designed for high single frequency performance is further analyzed and its normal incidence behavior is verified experimentally. Section 5 contains the conclusions drawn from this work.

2. Theory

2.1. AM realized by combination of 2D Helmholtz resonators and a sonic crystal

The structures proposed here comprise an infinite periodic arrangement of 2D Helmholtz resonators with a two-dimensional sonic crystal on top. They are intended for high absorption in the frequency range where wavelengths are much longer than the periodicity of the arrangement of resonators and the lattice parameter of the sonic crystal. The type of sonic crystal considered here is composed of cylindrical scatterers arranged in a hexagonal lattice with lattice parameter a. An example of a unit cell of the proposed type of AM is shown in Fig. 1a for a case where three resonators are included and five rows of cylinders compose the sonic crystal. The AM is realized through the repetition of the unit cell along the x axis.

A sonic crystal can be approximated as an equivalent fluid medium with homogenized sound speed, density and viscous attenuation coefficient in the presence of wavelengths that are much longer than the lattice parameter [17]. To obtain the homogenized speed of sound and density of isotropic structures, a model based on multiple-scattering theory was presented by Torrent et al. [19]. Alternative expressions

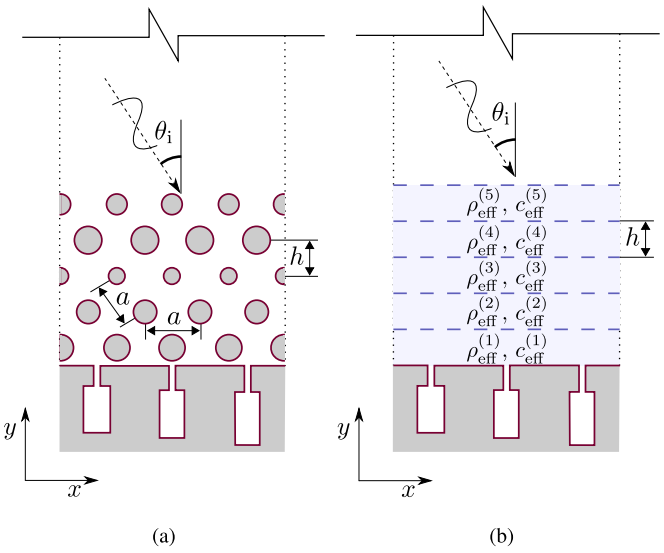

Fig. 1. Unit cell of an AM consisting of a periodic arrangement of three 2D Helmholtz resonators and a sonic crystal composed of five rows of cylinders arranged in a hexagonal lattice. The AM is realized through the repetition of the unit cell along the x axis. **(a)**: Unit cell with the arrangement of cylinders. **(b)**: Unit cell with equivalent fluid layers replacing the rows of cylinders. Each layer is equivalent to a row of cylinders. For the FEM models used to estimate the behavior of absorbers of this kind (see Section 2.3), the continuous boundary lines represent the boundaries with BLI boundary conditions, and the dotted lines represent boundaries with Floquet periodicity boundary conditions.

that yield comparable results but are also suitable to determine the homogenized properties of anisotropic structures have been proposed using multiple-scattering theory [20] and plane-wave expansion [21,22]. In turn, the model to estimate the viscous attenuation coefficient of isotropic or anisotropic structures presented by Ibarias et al. [23], uses plane-wave expansion.

The homogenized properties of the sonic crystal are dependent on the Bravais lattice, the speed of sound and density of air and the material of the scatterers, the cross-sectional shape of the scatterers, the lattice parameter a, and the filling fraction ff. The latter quantity is defined as the fraction of the domain that is occupied by the scatterers. For hexagonal lattices of cylindrical scatterers, the homogenized density and speed of sound are isotropic, and the filling fraction is related to the radius of the cylinders r_c and the lattice parameter a as

$$ff = \frac{2\pi}{\sqrt{3}}\left(\frac{r_c}{a}\right)^2. \tag{1}$$

If the lattice parameter is kept constant for all the rows of the crystal, but the radii of the cylinders is row-dependent, as shown in Fig. 1a, the crystal behaves as a multi-layer arrangement of fluid-like media. Each layer is equivalent to a row of cylinders, and it's effective properties are defined by the local ff value. Cylinder arrangements with spatially varying filling fraction have been used in previous works related to gradient index lenses in order to modify wave propagation [11,15,16]. Fig. 1b shows the geometry of the equivalent AM where the cylinders have been replaced with the fluid-like layers. The height of each of the equivalent layers is defined as the vertical center-to-center distance between cylinders of two subsequent rows, i.e. $h = a\cos(30°)$.

2.2. Analytic model of the AM

For an AM of the type shown in Fig. 1b, the surface of parallel 2D resonators can also be modeled as an homogeneous fluid-like medium in the frequency range where effects of the periodicity of the surface are not seen in the reflected sound field [9]. The condition for this is [24,25]

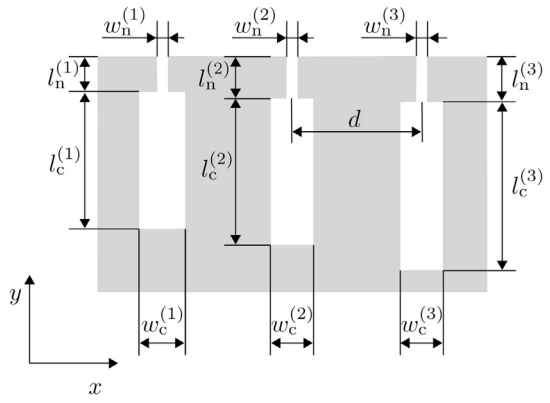

Fig. 2. Unit cell of a periodic arrangement with three 2D Helmholtz resonators.

$$f < \frac{c_0}{2w_{\text{cell}}}\,, \tag{2}$$

where c_0 is the speed of sound in air, $w_{\text{cell}} = d\,N_{\text{HR}}$ is the unit cell width, d is the distance between any two adjacent resonators and N_{HR} is the number of resonators in the unit cell. Then, the complete AM can be modeled as a serial assembly of the media corresponding to the equivalent rows of the sonic crystal and the surface of resonators.

To model the behavior of this equivalent system, we use the transfer matrix method (TMM) [26,27]. The transfer matrices that describe the behavior of the parallel arrangement of Helmholtz resonators and the sonic crystal as fluid-like layers are introduced in the next two subsections. Then, the expressions to obtain the global transfer matrix and the absorption coefficient of the AM are presented.

2.2.1. Transfer matrix of a parallel arrangement of 2D Helmholtz resonators

For reference, an example of a unit cell of the type of parallel arrangements of resonators considered throughout this paper is shown in Fig. 2. In the example, three different resonators are included.

The simplest case of a surface of this type is one including a single resonator per unit cell. Then, the transfer matrix is the result of an assembly in series of the outer end correction of the neck ($\mathbf{T}_{\Delta l_{\mathbf{n}}^{(\text{out})}}$), the neck ($\mathbf{T_n}$), the inner end correction of the neck ($\mathbf{T}_{\Delta l_{\mathbf{n}}^{(\text{in})}}$), and the cavity ($\mathbf{T_c}$) as $\mathbf{T_{HR}} = \mathbf{T}_{\Delta l_{\mathbf{n}}^{(\text{out})}}\mathbf{T_n}\mathbf{T}_{\Delta l_{\mathbf{n}}^{(\text{in})}}\mathbf{T_c}$, where

$$\mathbf{T}_{\Delta l_{\mathbf{n}}^{(\text{out})}} = \begin{bmatrix} 1 & \mathrm{i}k_{\text{n}}\Delta l_{\text{n}}^{(\text{out})} Z_{\text{n}} \\ 0 & 1 \end{bmatrix}\,, \tag{3}$$

$$\mathbf{T_n} = \begin{bmatrix} \cos(k_{\text{n}} l_{\text{n}}) & \mathrm{i}Z_{\text{n}}\sin(k_{\text{n}} l_{\text{n}}) \\ \mathrm{i}\dfrac{\sin(k_{\text{n}} l_{\text{n}})}{Z_{\text{n}}} & \cos(k_{\text{n}} l_{\text{n}}) \end{bmatrix}\,, \tag{4}$$

$$\mathbf{T}_{\Delta l_{\mathbf{n}}^{(in)}} = \begin{bmatrix} 1 & \mathrm{i}k_{\text{n}}\Delta l_{\text{n}}^{(\text{in})} Z_{\text{n}} \\ 0 & 1 \end{bmatrix}\,, \tag{5}$$

$$\mathbf{T_c} = \begin{bmatrix} \cos(k_{\text{c}} l_{\text{c}}) & \mathrm{i}Z_{\text{c}}\sin(k_{\text{c}} l_{\text{c}}) \\ \mathrm{i}\dfrac{\sin(k_{\text{c}} l_{\text{c}})}{Z_{\text{c}}} & \cos(k_{\text{c}} l_{\text{c}}) \end{bmatrix}\,, \tag{6}$$

k and Z are the wavenumber and characteristic impedance of the equivalent fluid representation of the slits respectively, and the subscripts n and c identify whether the physical quantities are related to the neck (n) or the cavity (c). In turn, $\Delta l_{\text{n}}^{(\text{in})}$ and $\Delta l_{\text{n}}^{(\text{out})}$ are the inner and outer end corrections of the neck.

The properties of the equivalent fluids that are representative of the neck and cavity sections are estimated using the effective density ($\rho_{\text{eff}}^{(\text{slit})}$) and bulk modulus ($B_{\text{eff}}^{(\text{slit})}$) from Stinson's expressions for plane wave propagation through narrow slits [9,28]. From these quantities, the characteristic impedance and wavenumber follow as

$$Z = \frac{d}{w}\left(\rho_{\text{eff}}^{(\text{slit})} B_{\text{eff}}^{(\text{slit})}\right)^{1/2}\,, \tag{7}$$

$$k = \omega\left(\frac{\rho_{\text{eff}}^{(\text{slit})}}{B_{\text{eff}}^{(\text{slit})}}\right)^{1/2}\,, \tag{8}$$

where w is the width of the slit. In these expressions, viscous and thermal losses happening at the boundaries of the slits are accounted for.

The inner and outer end corrections can be approximated using Smits and Kosten's derivations for surfaces with identical slit resonators under the assumption of constant pressure across the slit [9]. This assumption is not strictly true for a real system but is a common approximation used, for instance, in the Stinson model used here for the estimation of $\rho_{\text{eff}}^{(\text{slit})}$ and $B_{\text{eff}}^{(\text{slit})}$. These end corrections are defined as [29]

$$\Delta l_{\text{n}}^{(\text{in})} = \frac{\lambda}{\pi^2}\sum_{n=1}^{\infty}\frac{1}{R_n^{(\text{in})} n} F\left(n,-n,1,\sin^2\left(\frac{\pi w_{\text{n}}}{2w_{\text{c}}}\right)\right)\cdot \cdot \sin\left(\frac{n w_{\text{n}}\pi}{w_{\text{c}}}\right)\coth\left(kd R_n^{(\text{in})}\right)\,, \tag{9}$$

$$\Delta l_{\text{n}}^{(\text{out})} = \frac{\lambda}{\pi^2}\sum_{n=1}^{\infty}\frac{1}{R_n^{(\text{out})} n} F\left(n,-n,1,\sin^2\left(\frac{\pi w_{\text{n}}}{2d}\right)\right)\cdot \cdot \sin\left(\frac{n w_{\text{n}}\pi}{d}\right)\,, \tag{10}$$

where λ is the wavelength, $F(\cdot)$ is the hypergeometric function defined as

$$F(a,b,c,v) = \sum_{m=0}^{\infty}\frac{(a)_m (b)_m}{(c)_m}\frac{v^m}{m!}\,, \tag{11}$$

$$R_n^{(\text{in})} = \sqrt{\left(\frac{n\lambda}{w_{\text{c}}}\right)^2 - 1} \text{ and } R_n^{(\text{out})} = \sqrt{\left(\frac{n\lambda}{d}\right)^2 - 1}.$$

For unit cells containing more than one resonator, the transfer matrix of the parallel arrangement can be obtained using the formulation proposed by Verdière et al. [27]. It is valid for frequencies with wavelengths that are at least twice the width of the resonators' cavities, i.e. only when propagation in the normal direction to the surface is taking place. The elements of the 2×2 parallel transfer matrix $\mathbf{T_P}$ are defined as

$$T_{\text{P},11} = -\frac{Y_{22}^{(N_{\text{HR}})}}{Y_{21}^{(N_{\text{HR}})}}\,, \tag{12}$$

$$T_{\text{P},12} = \frac{1}{r}\frac{1}{Y_{21}^{(N_{\text{HR}})}}\,, \tag{13}$$

$$T_{\text{P},21} = r y_{12}^{(N_{\text{HR}})} - \frac{Y_{22}^{(N_{\text{HR}})}\left(\sum_{n=1}^{N_{\text{HR}}} r Y_{11}^{(n)} - \sum_{m=1}^{N_{\text{HR}}-1}\dfrac{Y_{12}^{(m)} Y_{21}^{(m)}}{Y_{22}^{(m)}}\right)}{Y_{21}^{(N_{\text{HR}})}}\,, \tag{14}$$

$$T_{\text{P},22} = -\frac{\sum_{m=1}^{N_{\text{HR}}-1} r\dfrac{Y_{12}^{(m)} Y_{21}^{(m)}}{Y_{22}^{(m)}} - \sum_{n=1}^{N_{\text{HR}}} r Y_{11}^{(n)}}{r Y_{21}^{(N_{\text{HR}})}}\,, \tag{15}$$

where N_{HR} is the number of Helmholtz resonators in the unit cell, $r = 1/N_{\text{HR}}$ is the fraction of the unit cell width that is occupied by each resonator, and $Y_{ij}^{(n)}$ is the ij-th element of the admittance matrix of the n-th resonator. This matrix is defined as

$$\mathbf{Y}^{(n)} = \frac{1}{T_{\text{HR},12}^{(n)}}\begin{bmatrix} T_{\text{HR},22}^{(n)} & T_{\text{HR},12}^{(n)} T_{\text{HR},21}^{(n)} - T_{\text{HR},22}^{(n)} T_{\text{HR},11}^{(n)} \\ 1 & -T_{\text{HR},11}^{(n)} \end{bmatrix}\,. \tag{16}$$

2.2.2. Transfer matrix of a 2D sonic crystal

As mentioned in Section 2.1, in the low-frequency range, the wave propagation through each of the rows of the two-dimensional sonic crystal shown in Fig. 1a can be modeled as happening inside a homogeneous fluid-like medium with properties depending on the local filling

fraction. Here, for each row l in the crystal, the speed of sound ($c^{(l)}_{\text{hom}}$), density ($\rho^{(l)}_{\text{hom}}$) and frequency-dependent viscous attenuation coefficient ($\gamma^{(l)}_{\text{hom}}$) are estimated using the expressions in the works by Krokhin et al. [21], Gumen et al. [22] and Ibarias et al. [23] respectively.

From the homogenized properties, the behavior of each row can be further approximated as a lossy fluid using complex effective sound speed ($c^{(l)}_{\text{eff}}$) and density ($\rho^{(l)}_{\text{eff}}$) values that include the viscous dissipation. They are related to the values from the homogenized models as [30]

$$c^{(l)}_{\text{eff}}(f) = \frac{\omega}{k^{(l)}_{\text{eff}}} = \frac{\omega}{\omega/c^{(l)}_{\text{hom}} - \mathrm{i}\gamma^{(l)}_{\text{hom}}(f)}, \tag{17}$$

$$\rho^{(l)}_{\text{eff}}(f) = \rho^{(l)}_{\text{hom}} \left(\frac{c^{(l)}_{\text{hom}}}{c^{(l)}_{\text{eff}}(f)} \right)^2, \tag{18}$$

where $\omega = 2\pi f$ is the angular frequency. The expression for the complex density yields a real effective bulk modulus value which is in line with the fact that only viscous losses are accounted for [26,28]. Note that, for a lossless fluid ($\gamma^{(l)}_{\text{hom}} = 0$), $\rho^{(l)}_{\text{eff}} = \rho^{(l)}_{\text{hom}}$ and $c^{(l)}_{\text{eff}} = c^{(l)}_{\text{hom}}$. Thermal losses have not been included in the proposed homogenized model for the sonic crystal, but their contribution to the total viscothermal losses in clusters of cylinders has been shown to be less than 10% [17]. It should be noted that thermal losses are indeed accounted for in the homogenized model of the arrangement of Helmholtz resonators, see Section 2.2.1.

The transfer matrix of each row of the sonic crystal is defined as [26]

$$\mathbf{T}^{(l)}_{\mathbf{r}} = \begin{bmatrix} \cos\left(k^{(l)}_y h\right) & \mathrm{i}\dfrac{Z^{(l)}}{\cos\theta^{(l)}} \sin\left(k^{(l)}_y h\right) \\ \mathrm{i}\dfrac{\cos\theta^{(l)}}{Z^{(l)}} \sin\left(k^{(l)}_y h\right) & \cos\left(k^{(l)}_y h\right) \end{bmatrix}, \tag{19}$$

where $Z^{(l)} = c^{(l)}_{\text{eff}} \rho^{(l)}_{\text{eff}}$, $\theta^{(l)}$ and $k^{(l)}_y = \left(\omega/c^{(l)}_{\text{eff}}\right)\cos\theta^{(l)}$ are respectively the characteristic impedance, the propagation angle, and the vertical component of the wavenumber inside the l-th row.

Contrarily to the case of the Helmholtz resonators, oblique propagation can take place inside the sonic crystal. From Snell's law, and considering the order from bottom to top of the sketch in Fig. 1b, the propagation angle inside the layer equivalent to the last row of cylinders, the N_{r}-th row, is found from the wavenumber in air $k_0 = \omega/c_0$, and the equality $k_0 \sin\theta_{\text{i}} = k^{(N_{\text{r}})} \sin\theta^{(N_{\text{r}})}$. For all the other rows, it is found from $k^{(l+1)} \sin\theta^{(l+1)} = k^{(l)} \sin\theta^{(l)}$, where $k^{(l)}$ and $\theta^{(l)}$ correspond respectively to the wavenumber and propagation angle inside of the l-th row of cylinders.

The transfer matrix of a crystal with N_{r} rows is then defined as

$$\mathbf{T_{cr}} = \mathbf{T}^{(N_{\text{r}})}_{\mathbf{r}} \mathbf{T}^{(N_{\text{r}}-1)}_{\mathbf{r}} \ldots \mathbf{T}^{(1)}_{\mathbf{r}}. \tag{20}$$

2.2.3. Analytic estimation of the absorption coefficient of the AM

The global matrix that describes the behavior of the complete AM shown in Fig. 1 is obtained as

$$\mathbf{T_G} = \mathbf{T_{cr}} \mathbf{T_P}. \tag{21}$$

Given that the AM is rigidly backed, the surface impedance follows as [26]

$$z_{\text{s}}(f, \theta_{\text{i}}) = \frac{T_{\text{G},11}(f, \theta_{\text{i}})}{T_{\text{G},21}(f, \theta_{\text{i}})}, \tag{22}$$

and the absorption coefficient is obtained as [31]

$$\alpha(f, \theta_{\text{i}}) = 1 - \left| \frac{\frac{z_{\text{s}}(f,\theta_{\text{i}})}{z_{\text{r}}} - 1}{\frac{z_{\text{s}}(f,\theta_{\text{i}})}{z_{\text{r}}} + 1} \right|^2 = 1 - \left| \frac{\frac{z_{\text{s}(f,\theta_{\text{i}})} \cos\theta_{\text{i}}}{\rho_0 c_0} - 1}{\frac{z_{\text{s}(f,\theta_{\text{i}})} \cos\theta_{\text{i}}}{\rho_0 c_0} + 1} \right|^2, \tag{23}$$

where ρ_0 is the density of air, and $z_{\text{r}} = \rho_0 c_0 / \cos\theta_{\text{i}}$ is the radiation impedance of an infinitely large surface.

2.3. Numerical model of the AM

The absorption performance of the specific designs presented and analyzed in the remainder of this paper is estimated using the analytic model presented in Section 2.2. Nevertheless, results from models of the surfaces based on the finite element method (FEM) are also used to verify the analytic results and visualize the field variables inside the absorbers. The commercial software package COMSOL Multiphysics® 6.0 is used to implement and solve the FEM models.

The numerical problem is solved for the acoustic pressure in the frequency domain using the Helmholtz equation and assuming a harmonic time-dependency $e^{\mathrm{i}\omega t}$. Two versions of the models are considered, one where the array of cylinders is represented by rigid solid inclusions (see Fig. 1a), and another one where each row of cylinders is replaced with a domain filled with a fluid with the effective properties defined in Eqs. (17) and (18) (see Fig. 1b).

The numerical domain consists of a unit cell of the absorber and a portion of the free field above it. Vertically, the domain is truncated using a perfectly matched layer (PML) placed 2.4 m above the absorber. In turn, Floquet periodicity boundary conditions are assigned at both sides of the outer field domain in order to simulate an infinite periodic surface. The viscous and thermal losses taking place in the vicinity of the boundaries of the resonators and the cylinders are accounted for using the boundary layer impedance (BLI) boundary condition [32,33]. These boundary conditions used are shown in Figs. 1a and 1b.

To estimate viscous and thermal losses using BLI, only the solution for the acoustic pressure is needed and fine meshing of the boundary layers is not necessary. Thus, this method uses less computation time and resources than the direct implementation of the full linearized Navier-Stokes equations. The expressions give a good estimation as long as there are no overlapping boundary layers, and the surface does not contain patterns in the order of the boundary layer thicknesses [33]. Previous works addressing the absorption of Helmholtz resonators have also used this method to account for boundary losses [9,34,35].

The angle-dependent incident plane wave is included in the model as an incident pressure field

$$p_{\text{inc}}(x, y) = |p_{\text{inc}}| \mathrm{e}^{-\mathrm{i}(k_{0,x} x - k_{0,y} y)}, \tag{24}$$

where

$$k_{0,x} = \frac{\omega}{c_0} \sin\theta_{\text{i}}, \tag{25}$$

$$k_{0,y} = \frac{\omega}{c_0} \cos\theta_{\text{i}}. \tag{26}$$

The reflected pressure field (p_{r}) is obtained by subtracting the incident pressure field from the total pressure field (p_{t}) that is found as the solution of the acoustic problem, i.e.

$$p_{\text{r}}(x, y) = p_{\text{t}}(x, y) - p_{\text{inc}}(x, y). \tag{27}$$

The absorption coefficient is calculated by estimating the ratio of the absorbed to incident acoustic power traveling across a horizontal line that spans the unit cell width and is placed 1.9 m above the surface. More details on the calculation method can be found in [9], which uses the same numerical approach to estimate the absorption coefficient of periodic surfaces of resonators.

The domain is discretized using quadratic Lagrange elements with maximum sizes of 2.8 mm, 12.5 mm and 30.9 mm in the domains related to the absorber, the outer field, and the PML respectively. In small gaps like the resonators necks and the space between the cylinders, a minimum of two elements was used for the domain discretization.

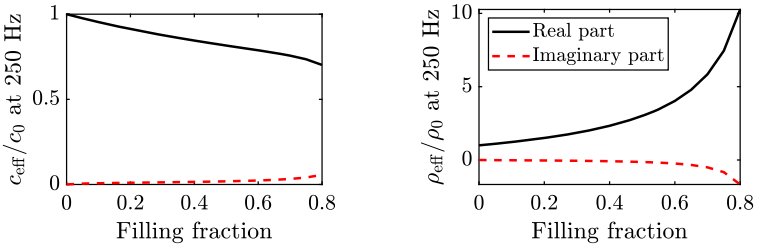

Fig. 3. Normalized complex effective properties at 250 Hz of a sonic crystal with a hexagonal lattice of cylindrical scatterers and parameter $a = 1.11$ cm.

3. Design by optimization

Our goal is to use the AMs proposed here to realize absorbers that can consistently achieve high absorption for a wide range of wave incidence directions. We consider a single-frequency and a multifrequency test case. The geometry of the AM that yields this behavior is defined by solving an optimization problem where the cost function (Φ) is calculated at each iteration using the analytic model based on TMM, see Section 2.2. The optimization problem is defined as

$$\min_{\boldsymbol{x}} \qquad \Phi = \frac{1}{N_\theta}\sum_{j=1}^{N_\theta}\left(1-\bar{\alpha}(\theta_{\text{i}}^{(j)},\mathbf{x})\right) \tag{28}$$

$$\text{subject to} \quad 0 \le x_k \le 1, \quad k = 1,...,4N_{\text{HR}}+N_{\text{r}},$$

where N_θ is the number of incidence angles accounted for in the cost function and $\bar{\alpha}$ is the absorption coefficient averaged over the frequencies of interest. The set of angles that is chosen in this paper comprises the range $0° \le \theta_{\text{i}} \le 60°$ discretized in steps of 15°, and the range $61° \le \theta_{\text{i}} \le 89°$ discretized in steps of 1°. With this set, the near-grazing region is given a higher weight within the cost function, as it is the region where it is more challenging to maintain a high absorption.

The design variables in $\mathbf{x}$ are interpolation variables defining the dimensions of the resonators ($k = 1,...,4N_{\text{HR}}$) and the filling fraction of each of the rows of cylinders ($k = 4N_{\text{HR}}+1,....,4N_{\text{HR}}+N_{\text{r}}$) between minimum and maximum allowable values as

$$w_{\text{n}}^{(k)} = w_{\text{n,min}} + x_k\left(w_{\text{n,max}} - w_{\text{n,min}}\right) \quad \text{for } k = 1,...,N_{\text{HR}}, \tag{29}$$

$$l_{\text{n}}^{(k-N_{\text{HR}})} = l_{\text{n,min}} + x_k\left(l_{\text{n,max}} - l_{\text{n,min}}\right) \quad \text{for } k = N_{\text{HR}}+1,...,2N_{\text{HR}}, \tag{30}$$

$$w_{\text{c}}^{(k-2N_{\text{HR}})} = w_{\text{c,min}} + x_k\left(w_{\text{c,max}} - w_{\text{c,min}}\right) \quad \text{for } k = 2N_{\text{HR}}+1,...,3N_{\text{HR}}, \tag{31}$$

$$l_{\text{c}}^{(k-3N_{\text{HR}})} = l_{\text{c,min}} + x_k\left(l_{\text{c,max}} - l_{\text{c,min}}\right) \quad \text{for } k = 3N_{\text{HR}}+1,...,4N_{\text{HR}}, \tag{32}$$

$$ff^{(k-4N_{\text{HR}})} = ff_{\text{min}} + x_k\left(ff_{\text{max}} - ff_{\text{min}}\right) \quad \text{for } k = 4N_{\text{HR}}+1,...,4N_{\text{HR}}+N_{\text{r}}, \tag{33}$$

where $ff^{(l)}$ is the filling fraction of the l-th row of cylinders.

For the specific design cases presented in the results section of this paper, the number of rows of cylinders (N_{r}) is set to 10, the defined box constraints for the AM parameters are shown in Table 1, and the numerical values of the properties of air are $\text{Pr} = 0.702$, $\gamma = 1.4$, $\mu = 1.814 \cdot 10^{-5}$ kg $\cdot$ m^{-1} $\cdot$ s^{-1}, $\text{P}_0 = 101320$ Pa, $\rho_0 = 1.204$ kg $\cdot$ m^{-3}, and $c_0 = 343.2$ m $\cdot$ s^{-1}, where μ, Pr, γ and P_0, are respectively the dynamic viscosity, Prandtl number, ratio of specific heats and static pressure of air.

Furthermore, the lattice parameter is fixed to a value of $a = 1.11$ cm. This yields a relationship between the normalized complex effective properties of the equivalent fluid and the filling fraction as shown in Fig. 3 for 250 Hz. The normalization is made with respect to the properties of air. In the calculation of these effective parameters, the material of the cylinders is defined arbitrarily but with the condition of high impedance contrast so that they behave as rigid elements. Specifically, the properties selected correspond to the ones of aluminum, i.e. the density and bulk modulus values were set to 2700 kg $\cdot$ m^{-3} and $51 \cdot 10^9$ Pa respectively.

Table 1
Box constraints for the parameters of the AM designed for broad angle range of high absorption. All the quantities referring to dimensions are given in mm.

	w_n	l_n	w_c	l_c	ff
min.	0.8	8.0	20.0	40.0	0
max.	1.2	30.0	90.0	150.0	0.8

The maximum allowable value of the filling fraction in Table 1 ensures that there is no overlapping of the viscous boundary layers of adjacent scatterers. The latter is a condition of validity of the homogenization model for the viscous attenuation constant inside the sonic crystal [23]. More explicitly, the upper box constraint of $ff = 0.8$ is set so that the extent of the viscous boundary layers in the frequency range starting from 100 Hz is below the overlapping limit.

To solve the optimization problems, the sequential quadratic programming (SQP) algorithm implemented in the *fmincon* function of MATLAB® [36] is used. SQP is an effective method to solve constrained non-linear optimization problems [37] and has been used in previous works to design absorbers based on resonators [7,9,38,39]. Here, the sensitivities of the objective function at each iteration are estimated using forward finite differences with a step size of 1.49×10^{-8}. Given that the solution method is gradient-based, solutions are found using various initial guesses for each of the problems. This minimizes the possibility of ending up with a solution that is a poorly performing local minimum. The final solution is selected as the one for which the final cost function reached a lower value.

4. AMs for sound absorption over a broad range of wave incidence angles

4.1. AM optimized for single frequency performance

The aim of this first test case is to design an AM for sound absorption over a broad range of incidence angles at a single frequency of 250 Hz. For this purpose, the parameters for an absorber with only one resonator per unit cell and a unit cell width of $w_{\text{cell}} = d = 10$ cm are optimized using 10 random initial guesses. Calculations are performed on a desktop computer with a 10 core Intel® Xeon® W-2155 CPU, 128 GB of RAM and a 512 GB SSD M.2 hard drive. When solving the problem, the solution time including the 10 initial guesses is 13 minutes. This limited solution time highlights the efficiency of using the analytic

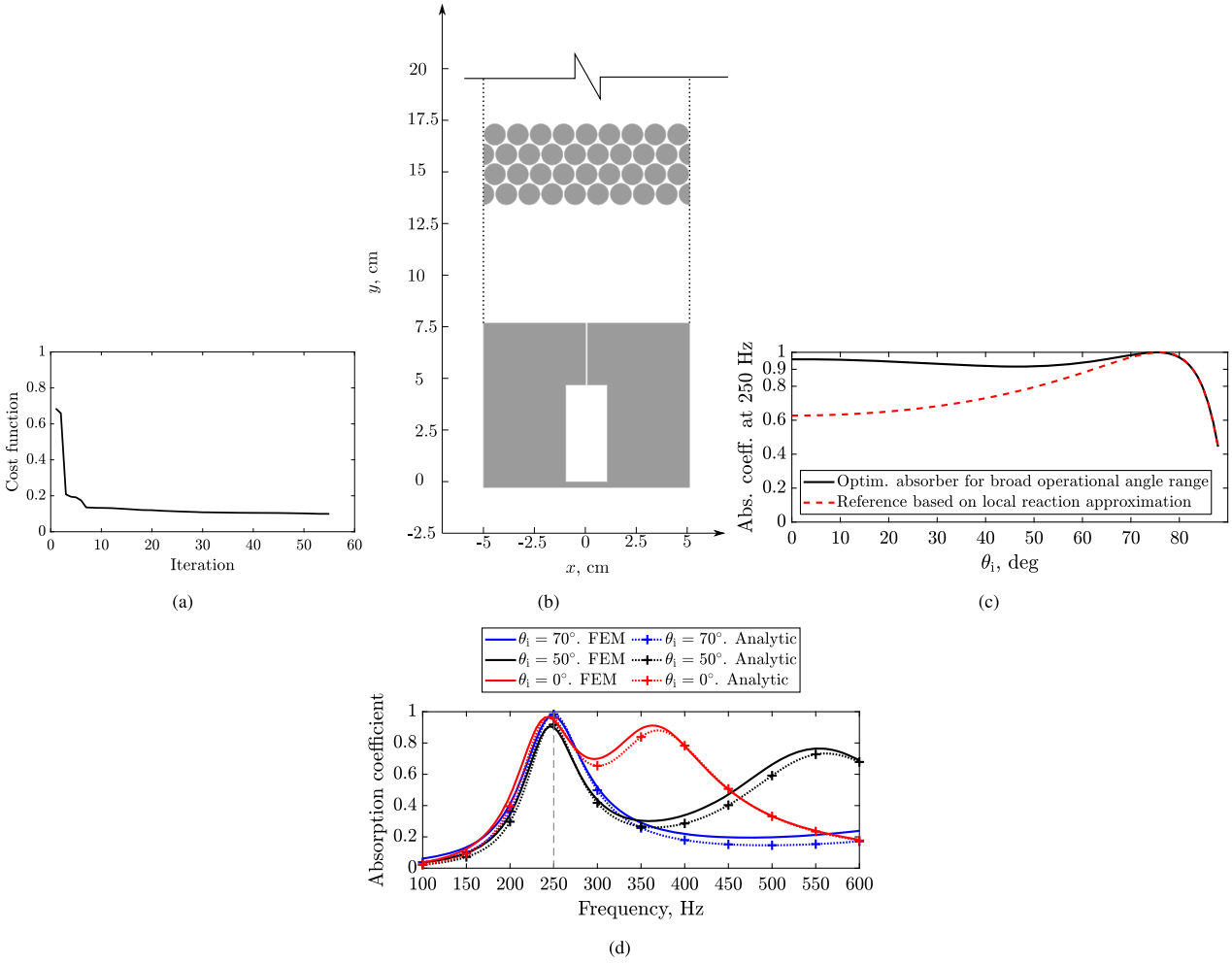

Fig. 4. Optimized AM for broad angle range of high absorption at 250 Hz. **(a):** Convergence of the optimization problem. **(b):** Geometry of a unit cell. **(c):** Absorption coefficient at 250 Hz as a function of the incidence angle calculated using the analytic model presented in Section 2.2. It is compared to the performance that would be achieved by a surface approximated as locally reacting. **(d):** Absorption coefficient as a function of the frequency for selected incidence angles calculated using the analytic and FEM models presented in Sections 2.2 and 2.3 respectively.

Table 2
Optimized parameters of the AM with broad angle range of high absorption at 250 Hz. The dimensions of the resonator are given in mm.

w_n	l_n	w_c	l_c	d	$ff^{(1)}$	$ff^{(2)}$	$ff^{(3)}$	$ff^{(4)}$	$ff^{(5)}$	$ff^{(6)}$	$ff^{(7)}$	$ff^{(8)}$	$ff^{(9)}$	$ff^{(10)}$
0.8	30	20	46.8	100	0	0	0	0	0	0	0.8	0.8	0.8	0.8

model of the AM in Section 2.2 to estimate's the surface's absorption in the optimization.

The difference between the lowest and highest objective function value obtained after solving for all the initial guesses is 0.01. Among the different solutions obtained, there is a maximum variation of 21% in the dimensions of the resonator. The largest deviations are seen in the dimensions of the cavity. Furthermore, the optimized ff values for all the rows, and for all the solutions, only take values of 0 or 0.8, i.e. the minimum and maximum allowable values respectively. The only common values for all solutions are $ff^{(1)} = 0$, $ff^{(9)} = 0.8$ and $ff^{(10)} = 0.8$.

The small variation in the values of the final cost function despite the geometrical differences means that broad angular absorption is not exclusively obtained with a single specific design. Furthermore, the fact that all the optimized ff values only correspond to either the lower or upper box constraints, suggests that increasing the maximum allowable value constraint for this variable might be beneficial. Nevertheless, as stated in Section 3, this upper box constraint ensures the condition for validity of the homogenization model.

The AM parameter values of the chosen solution can be seen in Table 2, the convergence of the optimization problem is shown in Fig. 4a, and the optimized geometry can be seen in Fig. 4b. The optimized cylinder radii are obtained from the optimized values of ff for each row and the relationship shown in Eq. (1). The final geometry consists of a sonic crystal with 4 rows of cylinders with an equal filling fraction (0.8), i.e. 4 rows of cylinders of 0.52 cm radii, that is separated from the resonator surface by an air cavity that is 5.7 cm high. The air cavity of the design is a consequence of the fact that the optimized ff values for the first six rows of the crystal are equal to zero.

The absorption coefficient at 250 Hz as a function of the incidence angle is shown in Fig. 4c. It can be seen that the optimized AM achieves consistently high absorption over a broad range of incidence angles. Namely, it yields absorption coefficient values above 0.9 for $0° \leq \theta_i \leq 83°$, well beyond the capabilities of locally reacting acoustic absorbing materials, used here as a reference. Locally react-

ing absorbing materials have a surface impedance that is independent of the incidence angle, and several types of acoustic absorbers have a behavior that can be approximated as such. This group includes the surfaces composed of quarter-wavelength or Helmholtz resonators as used in this work, and some porous materials [1]. A locally reacting absorbing material that is designed to achieve maximum absorption at angles approaching grazing incidence loses absorption at other angles due to the strong dependence of the radiation impedance with angle [9], see Eq. (23). To illustrate the improved performance of the proposed AM, a reference curve has been included in Fig. 4c showing the angle-dependent absorption coefficient of a locally reacting absorber which has the same performance at large incidence angles ($\theta_i \geq 70°$), and maximum absorption at 76°, i.e. the same angle of maximum absorption as the optimized design. The reference absorption curve is calculated from Eq. (23) and using a surface impedance value $z_s = \rho_0 c_0 / \cos(76°)$. The superiority of the designed AM is obvious for narrow incidence angles, with the largest difference at normal incidence, where the locally reacting absorber achieves an α value of 0.63, whilst the proposed design achieves an α value of 0.96.

The enhanced angular performance of the metasurface presented is a result of the coupled behavior between the surface of resonators and the sonic crystal, see Section 4.1.1 for details. Alternative attempts were made to achieve broad angular absorption using a wide range of porous absorbers instead of the sonic crystal. The use of porous materials helped increase the frequency range of high absorption, but did not yield a significant improvement in the angular performance. This emphasizes the advantage of using the cluster of cylinders to tailor wave propagation properties. The detailed results from the alternative study are out of the scope of this publication but are available in [40].

A practical drawback of the proposed absorber with respect to e.g. a more common type of AM with only Helmholtz resonators is its increased thickness. The total thickness of the proposed absorber is 17.3 cm, of which 9.7 cm correspond to the added cylinder arrangement and the air space behind it. This could be a limitation for applications with strict spatial limitations. Nonetheless, the thickness is still around 1/8 times the wavelength of the optimization frequency, which is half the space that would approximately be needed for a traditional porous absorber to achieve a high absorption coefficient. This is, considering the common practical reference that the thickness of a porous absorber backed by a rigid surface should be at least around 1/4 times the wavelength with the aim that a maximum of the particle velocity, and therefore high viscous dissipation, take place inside the material [1].

Reducing the thickness of the structure on top of the resonators would affect the performance of the absorber as its behavior is dependent on resonant phenomena inside this space (as will be discussed in the next section). Nevertheless, the Helmholtz resonators can be compacted further using strategies proposed in previous works like coiled geometries [41,39,42] and/or embedded necks [43–45].

To verify the results obtained using the analytic model presented in Section 2.2, Fig. 4d compares the estimated absorption coefficient values as a function of frequency using the analytic and FEM models. The behavior for three incidence angles is shown, and it can be seen that there is a good agreement between the two methods. The FEM models account for both viscous and thermal losses. Therefore, the good agreement between the analytic and numerical results shows that the homogenization model, which does not include thermal losses in the cluster of cylinders, is a good approximation to describe the behavior of the AM.

4.1.1. Acoustic behavior of the proposed AM

To gain insight into the mechanisms that allow for a broad angular absorption, relevant acoustic properties of the AM are shown in the first row of Fig. 5. Namely, the absorption coefficient as a function of the incidence angle and frequency is shown in Fig. 5a, and the real and imaginary parts of the normalized surface impedance are shown in a logarithmic scale in Figs. 5b and 5c respectively. The normalization is done using the radiation impedance. The normalized surface impedance evaluates the degree of coincidence between the outer field and the absorber at their interface. As can be seen in Eq. (23), total absorption is obtained when the real and imaginary parts of the normalized surface impedance are equal to one and zero respectively.

The proposed AM has two resonance frequencies for most angles and in the frequency range considered in Fig. 5. This can be seen in Fig. 5a, where there is more than one absorption peak for most angles, and from the zero crossings of the normalized reactance shown in Fig. 5c. Note that, since a logarithmic scale is used in Fig. 5c, the zero crossings correspond to the regions with low negative values.

Plots of the absorption coefficient, and real and imaginary parts of the normalized surface impedance of a surface with only the resonators, and a surface with the sonic crystal and the air-filled space placed above a rigid plane are included in the middle and bottom row of Fig. 5 respectively. The results are obtained by setting respectively $\mathbf{T_G} = \mathbf{T_P}$ and $\mathbf{T_G} = \mathbf{T_{cr}}$ in Eq. (21) for the surface with only the resonators and the surface with the sonic crystal and the air-filled cavity. These additional figures show that the first resonance frequency of the AM, which appears in the vicinity of the optimization frequency, is characteristic of the surface with resonators and is independent of the incidence angle. The second resonance is characteristic of the sonic crystal and the air space below it. It appears at an angle-dependent frequency due to the oblique propagation that can take place inside this particular system. When the systems are coupled, the position of the absorption peaks with respect to the peaks of the independent systems have a slight shift, see Figs. 5a, 5d and 5g.

The real part of the sound pressure over the designed absorber and for frequencies near the two resonances is shown in Fig. 6. These results are obtained using the FEM models described in Section 2.3. The upper row shows the pressure distribution for three unit cells with the cylinders. To improve the visualization, in the bottom row, the acoustic pressure is shown using the equivalent fluid media representation of the rows of cylinders. Figs. 6a and 6d show the sound pressure for 240 Hz and considering normal incidence (corresponds to the point indicated with a black dot in Figs. 5a, 5b and 5c), which is a frequency near the Helmholtz resonance. Consequently, a higher sound pressure can be seen in the resonators cavities.

Figs. 6b and 6e show the pressure near the second resonance and for $\theta_i = 0°$, namely at 365 Hz (corresponds to the point indicated with a black 'x' in Figs. 5a, 5b and 5c). It can be seen that this is a mode that extends over the vertical space occupied by the air cavity and the cylinders. Given that oblique propagation can take place across the space occupied by the cylinders and the air cavity, see Section 2.2.2, waves that meet the AM surface at non-normal angles will travel with a horizontal component in this region. Then, the projection of the wavelength in the vertical direction will become larger, so the same vertical mode seen for normal incidence (in Figs. 6b and 6e) will appear at higher frequencies. An example of this is included in Figs. 6c and 6f, where the pressure is shown for $f = 555$ Hz and $\theta_i = 50°$ (indicated with a black triangle in Figs. 5a, 5b and 5c). The latter explains the angle-dependent position of the second resonance of the system.

In addition to the two resonances of the AM, a third characteristic is the anti-resonance indicated with an arrow in the figures corresponding to the real and imaginary parts of the normalized surface impedance of the AM, Figs. 5b and 5c respectively. It is an effect of the coupling of the two systems which appears between two resonances and causes a localized increase of the surface resistance as can be seen in Fig. 5b. Even though the absorption coefficient drops at the anti-resonance, it plays an important role in broadening the angular response of the AM. From Fig. 5b, it can be seen that the position of the antiresonance in the vicinity of the optimization frequency and its angular dependency keep the normalized resistance near a value of one (zero on a logarithmic

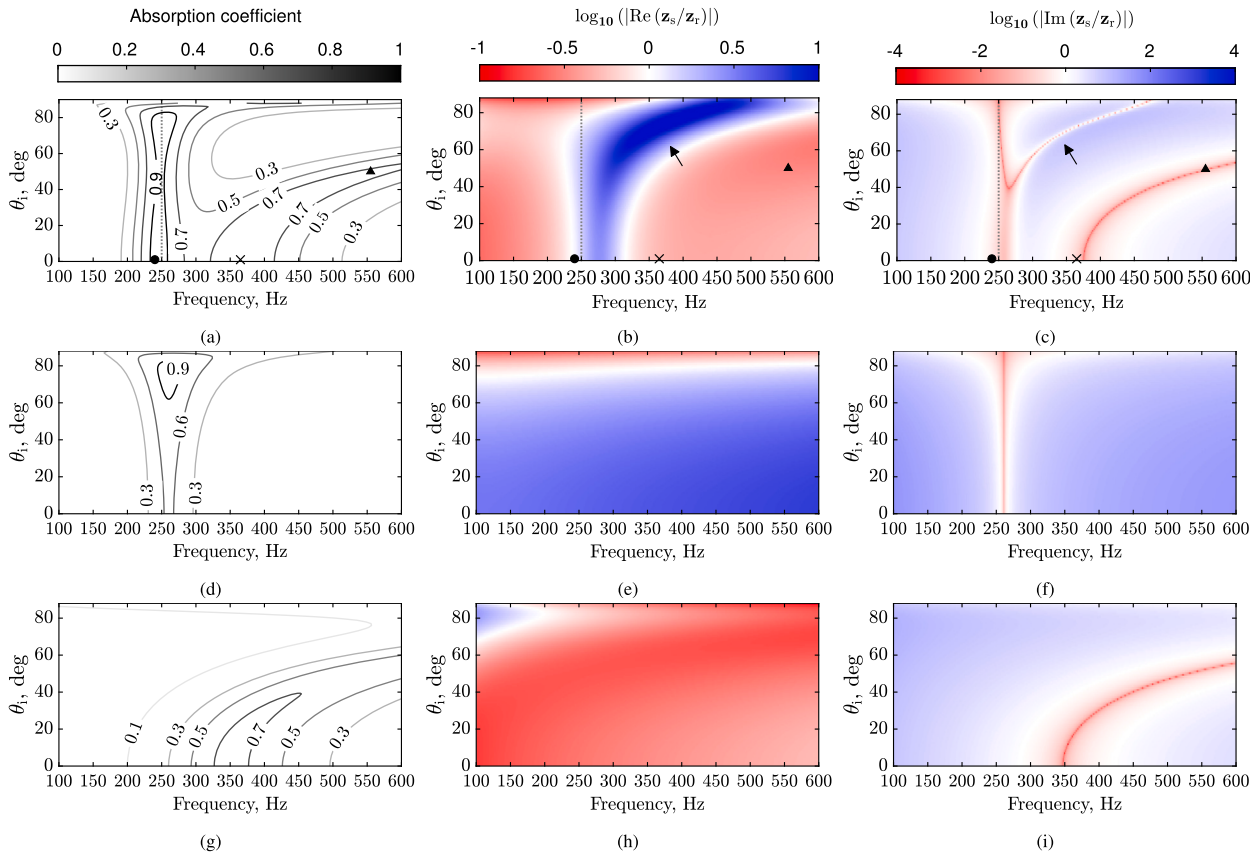

Fig. 5. Absorption coefficient (in linear scale) and real and imaginary parts of the normalized surface impedance (in logarithmic scale) of the AM with broad angle range of high absorption (**top row**), an absorber comprised only of the resonators (**middle row**), and an absorber comprised of the array of cylinders and the air space behind them with a rigid-surface backing (**bottom row**). The dotted vertical line in the top row figures indicates the frequency used for the optimization, the circle, cross and triangle symbols indicate the cases for which the acoustic pressure is visualized in Fig. 6, and the arrow identifies the antiresonance of the system.

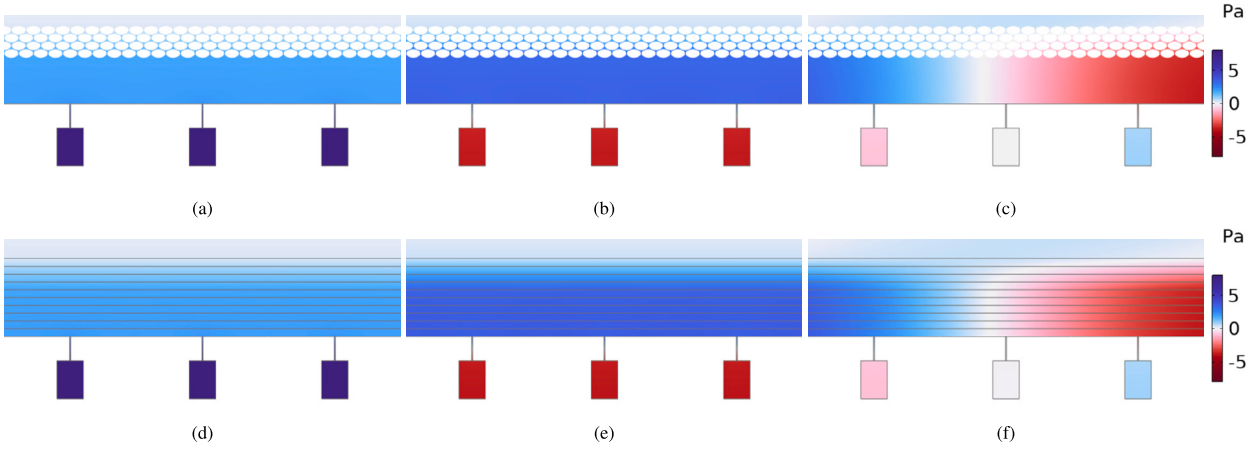

Fig. 6. Real part of the sound pressure over three unit cells of the AM optimized for broad angle range of high absorption at 250 Hz. **Left column:** at $f = 240$ Hz and $\theta_i = 0°$. **Middle column:** at $f = 365$ Hz and $\theta_i = 0°$. **Right column:** at $f = 555$ Hz and $\theta_i = 50°$. **Top row:** Results from the FEM model with the physical cylinders. **Bottom row:** Results from the FEM model using the equivalent fluid description of the array of cylinders. The horizontal lines show the limits between fluid layers.

scale) at the frequency of interest and over an extended range of angles.

In summary, in the vicinity of the optimization frequency, the first resonance of the AM generates a vanishing value of the surface reactance, and the anti-resonance maintains a high degree of coincidence between the surface resistance and the radiation impedance for a broad range of angles. As previously discussed, and shown in Eq. (23), these two conditions lead to a high absorption coefficient, which explains the broad angular absorption of the proposed surface.

4.1.2. *Experimental validation*

An experimental validation of the AM performance is done using measured values of the normal incidence absorption coefficient of 3D printed samples following the standardized procedure ISO 10534-2 [46]. The test equipment comprises an impedance tube from Acoustic Engineering Dresden (Dresden, Germany) of circular cross section with an internal diameter of 10 cm, and two $1/4''$ microphones placed 22.5 cm apart. With this setup, the frequency range of validity for the measurements is 77 Hz $\leq f \leq$ 688 Hz.

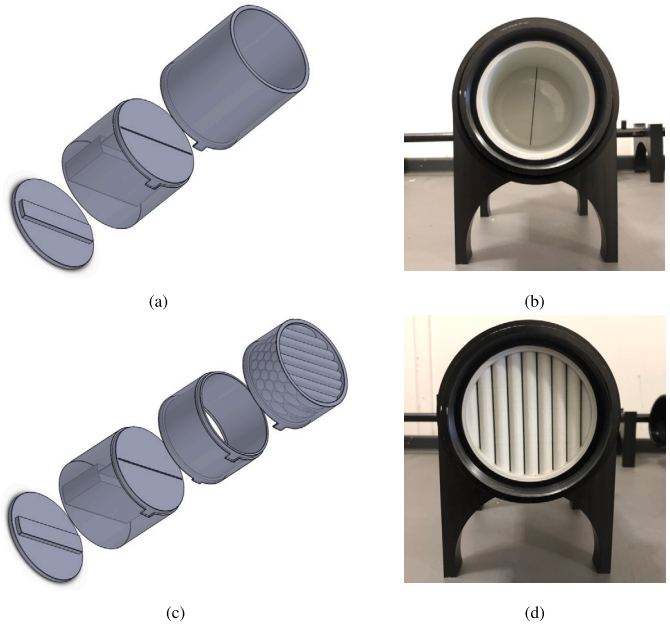

Fig. 7. 3D printed samples measured using an impedance tube with an inner diameter of 10 cm. **(a)** and **(b):** Exploded view and picture of the sample with only the resonator. **(c)** and **(d):** Exploded view and picture of the sample of the AM optimized for broad angle range of high absorption at 250 Hz. The pictures of the samples show them as installed in the impedance tube.

The measurement samples are 3D printed using a fused deposition modeling (FDM) extrusion printer BCN3D (Barcelona, Spain) Epsilon W23, polylactic acid (PLA) filament, a layer thickness of 0.2 mm, and a nozzle diameter of 0.4 mm. Two samples are measured, one that includes only the resonator of the optimized AM, and one that includes the resonator and the cylinders. The samples have a cylindrical shape with an outer diameter corresponding to the inner diameter of the impedance tube, i.e. 10 cm. A 5 mm thick ring is printed around the perimeter of the samples in order to keep the cylindrical shape and the sonic crystal scatterers in the right position above the resonator. The absorbers are realized as assemblies of independently printed parts. Exploded views that show the constitutive parts are shown in Figs. 7a and 7c, and pictures of the samples installed inside the impedance tube are shown in Figs. 7b and 7d. Preliminary experimental results showed that deviations in the dimensions of the printed parts with respect to the nominal dimensions had a significant impact on the measured absorption. Narrow geometries such as the neck of the resonator and the gap between adjacent cylinders were especially sensitive to this. To minimize this effect, the parts corresponding to the resonator and the cylinders are printed several times, each time adjusting the nominal dimensions in the CAD model in order to compensate for the deviations in the dimensions of the printed parts.

Every sample is measured at least three times. Each time, the sample is removed from the tube and reinstalled. The normal incidence absorption coefficient values reported here correspond to the averages over the number of measurements. The maximum difference in the absorption coefficient values measured at a given frequency is of 0.06, but the larger deviations appear for the frequency range above the two resonances of the system, namely in the range where $f > 480$ Hz. Below this frequency range, the maximum deviation is less than 0.03.

The cylindrical 3D geometry of the sample influences the performance of the original 2D design as there is a change in the ratio of open area of the surface and of the unit cell width of the absorber due to the outer ring around the samples. Furthermore, the presence of walls around the sonic crystal changes its effective properties [14]. For that reason, additional 3D FEM calculations are made using a model that reproduces the impedance tube setup. The acoustic source is modeled as a

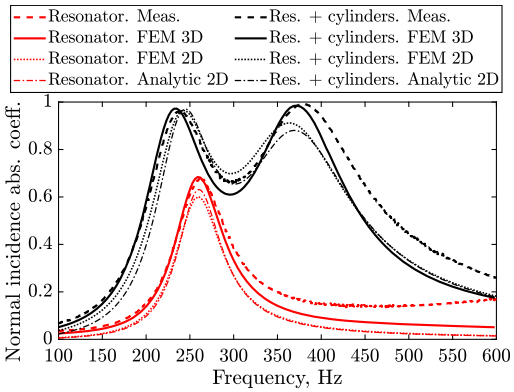

Fig. 8. Experimental verification of the normal incidence absorption coefficient of the AM optimized for broad angle range of high absorption at 250 Hz.

normal acceleration boundary condition, the acoustic pressure values at the positions corresponding to the microphones are extracted, and the absorption coefficient is calculated using the transfer function method described in the standard ISO 10534-2 [46]. Viscothermal losses happening along the resonator, cylinders and impedance tube walls, are accounted for in the FEM model using BLI boundary conditions. The maximum element sizes for the domains related to the samples being measured and the impedance tube are 4.1 mm and 7.4 mm respectively. In small gaps like the resonator's neck and the space between the cylinders, a minimum of two elements are used for the domain discretization.

Fig. 8 shows the normal incidence absorption coefficient values obtained from the measurements, the 3D FEM model, and the 2D FEM and analytic models. There is a good agreement between the 3D simulated and measured results, and the increase in the normal incidence absorption coefficient of the surface of resonators when including the sonic crystal is verified experimentally. Nevertheless, there is a slight deviation in the resonance frequencies and an increase in the absorption at frequencies that do not correspond to any resonance. The highest differences in absorption coefficient for a given frequency occur around 277 Hz and 451 Hz, where deviations up to 0.07 and 0.15 can be seen respectively. The deviations can be explained by manufacturing tolerances and roughness of the surfaces due to the 3D printing technology used [47,48]. Another source for increased absorption can be the vibration of the samples which are realized as an assembly of independently printed parts. The estimated 2D absorption coefficients are shown in Fig. 8 for reference. Some deviation from the 3D performance is expected due to the aforementioned effect of the cylindrical geometry of the experimental sample and the walls around the sonic crystal. The curves showing the absorption coefficient for the 2D absorber with the resonators and the cylinders, correspond to the absorption coefficient curves for $\theta_i = 0$ in Fig. 4d.

4.2. AM optimized for octave-band performance

In order to demonstrate an absorber with broad angle range of high absorption that is effective over an octave frequency band, a surface that includes six Helmholtz resonators per unit cell is optimized for the octave band centered at 250 Hz, i.e. for 177 Hz $\leq f \leq$ 354 Hz. The increased number of resonators allows to extend the frequency range of high absorption of the surface. For this test case, the spacing between resonators is defined as an additional design variable with upper and lower constraint values of 0.05 m and 0.08 m respectively. The upper limit guarantees that the unit cell width is narrow enough to avoid periodicity effects within the octave-band of interest, see Eq. (2). Furthermore, to prevent that the resonators become wider than their assigned space, six additional constraints are defined for the optimization problem as $w_c^{(i)} - d + 0.005\text{m} \leq 0$ for $i = 1, \ldots, 6$.

Table 3
Optimized parameters of the AM with broad angle range of high absorption over the 250 Hz octave-band. The dimensions of the resonators are given in mm.

i	$w_n^{(i)}$	$l_n^{(i)}$	$w_c^{(i)}$	$l_c^{(i)}$	d	$ff^{(1)}$	$ff^{(2)}$	$ff^{(3)}$	$ff^{(4)}$	$ff^{(5)}$	$ff^{(6)}$	$ff^{(7)}$	$ff^{(8)}$	$ff^{(9)}$	$ff^{(10)}$
1	0.8	17.0	36.8	40.0	50.0	0	0	0	0	0	0	0	0.8	0.8	0.8
2	1.2	8.0	45.0	41.0											
3	0.8	15.1	29.3	40.0											
4	0.8	9.4	45.0	120.6											
5	1.2	8.0	45.0	41.0											
6	0.8	17.3	45.0	46.6											

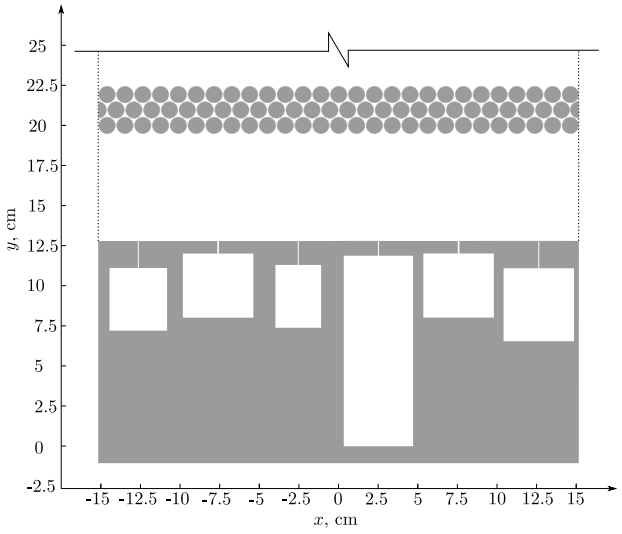

Fig. 9. Unit cell of the optimized AM for broad angle range of high absorption over the 250 Hz octave-band.

The problem is solved using 5 different random initial guesses and all the solutions found from the initial guesses are the same except for one. It takes four hours and seven minutes to solve the problem using the five different initial guesses. The highest variability in the resonators optimized dimensions across the solutions obtained is 23%. The difference in the geometry of the optimized sonic crystals is in the value of the filling fraction of the 7-th row of the crystal: for the 4 identical solutions $ff^{(7)} = 0$ (no cylinders), for the nonidentical solution $ff^{(7)} = 0.8$. Nevertheless, similar to the single frequency case, a small variability between the final cost function values is seen, namely, the maximum difference is of 0.012.

The optimized values of the parameters of the surface are presented in Table 3, and the geometry of the design is presented in Fig. 9. It can be seen that for this test case, the optimized geometry also includes an upper region of closely packed cylinders followed by an air cavity between the cylinders and the resonators. Furthermore, there is a resonator that significantly increases the thickness of the surface. As previously discussed for the single frequency test case, the surface of resonators can be compacted further by using coiled geometries and/or embedded necks.

The octave-band average absorption coefficient as a function of the incidence angle can be seen in Fig. 10a, and the absorption coefficient as a function of frequency for all and selected incidence angles is shown in Figs. 10b and 10c respectively. The results in Figs. 10a and 10b are obtained using the analytic model, the results in Fig. 10c are obtained both with the analytic and FEM models. Small differences in the position of the resonances can be seen between the analytic and FEM results. These can be explained by the fact that the expression used for the outer end corrections of the resonators does not take into account the evanescent coupling between resonators tuned to different frequencies.

The proposed AM can achieve an octave-band averaged absorption coefficient that is equal or higher than 0.9 for the angle range up to 83°, see Fig. 10a, which shows that the proposed type of absorber is also suitable for multifrequency acoustic reflection control over a wide range of incidence angles. Similar to the case of the single-frequency absorber, the multifrequency case outperforms the reference curve describing the behavior of a material with angle-independent surface impedance with maximum octave-band average absorption at the same incidence angle as the optimized surface. For normal incidence, the AM achieves an absorption coefficient of 0.93 which is much higher than what can be achieved by the reference, i.e. $\alpha = 0.63$.

5. Conclusions

In this paper, a type of AMs that can achieve high absorption coefficient values over a broad range of wave incidence angles has been proposed. These absorbers are realized through a periodic surface with a unit cell that combines a parallel arrangement of 2D Helmholtz resonators and a sonic crystal. The combination of the resonators as effective low frequency absorbers, and the sonic crystal which allows to control oblique wave propagation inside the absorber, makes it possible to tailor the AM behavior in accordance to changes in the radiation impedance as the incidence angle varies. The proposed surfaces have been shown to achieve high acoustic absorption over a range of incidence angles that is significantly broader than the angle range of high absorption of absorbers that can be approximated as locally reacting.

An analytic model was presented to estimate the low frequency performance of the AMs, and was used to efficiently optimize designs to achieve broad angular absorption at defined sets of frequencies. Specific designs were optimized for single frequency and octave-band absorption, and their performance was verified using a finite element model. Moreover, the experimental normal incidence absorption coefficient of a 3D printed sample of the AM designed for single-frequency excitation showed a very good agreement with the simulated values.

The present study is limited to a two-dimensional analysis, and only the variation with respect to the elevation angle is considered. The effect of changes in the azimuth angle should be considered to validate the performance of the surfaces under consideration in three-dimensional sound fields.

CRediT authorship contribution statement

Diana Maria Garza-Agudelo: Conceptualization, Investigation, Methodology, Software, Validation, Writing – original draft. **Vicente Cutanda Henriquez:** Conceptualization, Supervision, Writing – review & editing. **Cheol-Ho Jeong:** Conceptualization, Supervision, Writing – review & editing. **Peter Risby Andersen:** Conceptualization, Supervision, Writing – review & editing. **Martin Ibarias:** Conceptualization, Investigation, Writing – review & editing. **José Sanchez-Dehesa:** Conceptualization, Supervision, Writing – review & editing. **Frieder Lucklum:** Resources, Writing – review & editing.

Declaration of competing interest

The authors declare the following financial interests/personal relationships which may be considered as potential competing interests:

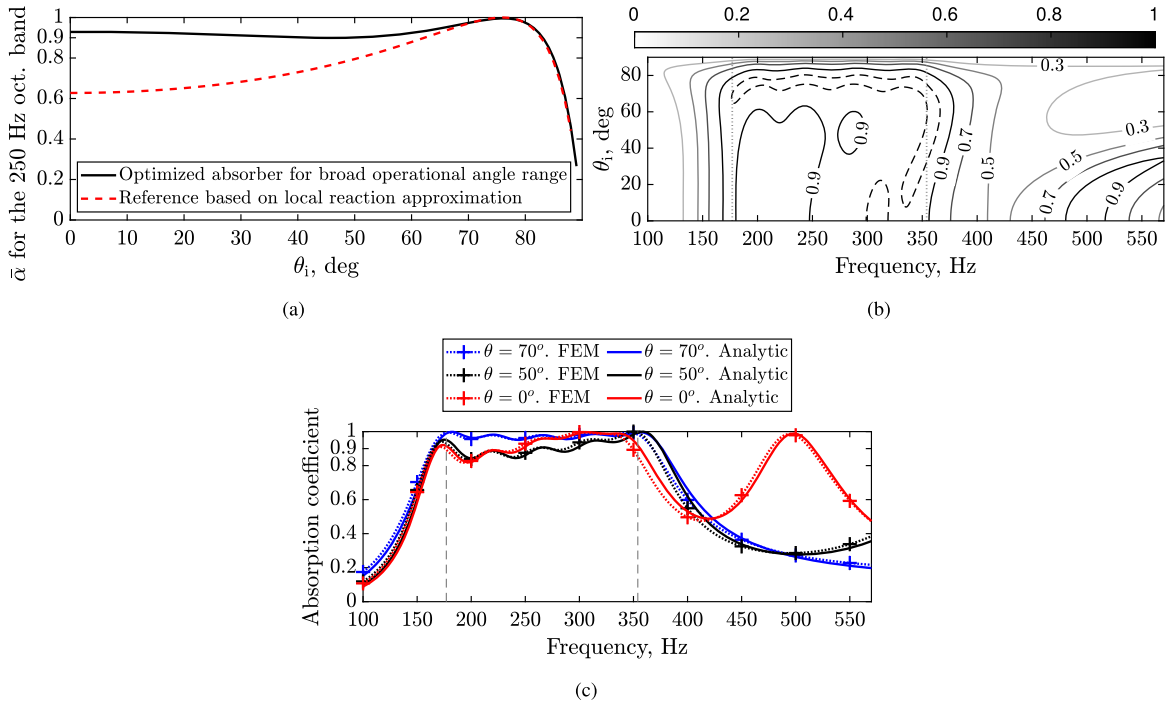

Fig. 10. Absorption coefficient of the AM for broad angle range of high absorption over the 250 Hz octave-band. **(a):** Absorption coefficient as a function of the incidence angle calculated using the analytic model presented in Section 2.2. It is compared to the performance that would be achieved by a surface that can be approximated as locally reacting. **(b):** Absorption coefficient as a function of frequency and the incidence angle calculated using the analytic model presented in Section 2.2. The dashed line corresponds to the 0.99 isocontour. **(c):** Absorption coefficient as a function of frequency for selected incidence angles calculated using the analytic and FEM models presented in Sections 2.2 and 2.3 respectively.

Jose Sanchez-Dehesa reports financial support was provided by Spain Ministry of Science and Innovation. Professor Cheol-Ho Jeong is an associate editor for Applied Acoustics.

Data availability

Data will be made available on request.

Acknowledgements

This research was carried out within the Signature project, a collaboration between the Technical University of Denmark and the Korea Advanced Institute of Science and Technology (KAIST) in the research of metamaterials. José Sanchez-Dehesa acknowledges the financial support by the Spanish Ministerio de Ciencia e Innovación through the grant PID2020-112759GB-I00 funded by MCIN/AEI/10.13039/501100011033.

References

[1] D'Antonio P, Cox TJ. Acoustic absorbers and diffusers: theory, design and application. 3rd ed. CRC Press; 2017.
[2] Hodgson M, Wareing A. Comparisons of predicted steady-state levels in rooms with extended- and local-reaction bounding surfaces. J Sound Vib 2008;309:167–77. https://doi.org/10.1016/j.jsv.2007.06.069.
[3] Zhang X, Qu Z, Wang H. Engineering acoustic metamaterials for sound absorption: from uniform to gradient structures. iScience 2020;23:101110. https://doi.org/10.1016/j.isci.2020.101110.
[4] Gao YX, Lin YP, Zhu YF, Liang B, Yang J, Yang J, et al. Broadband thin sound absorber based on hybrid labyrinthine metastructures with optimally designed parameters. Sci Rep 2020;10:10705. https://doi.org/10.1038/s41598-020-67688-x.
[5] Peng X, Ji J, Jing Y. Composite honeycomb metasurface panel for broadband sound absorption. J Acoust Soc Am 2018;144:EL255–61. https://doi.org/10.1121/1.5055847.
[6] Yang M, Chen S, Fu C, Sheng P. Optimal sound-absorbing structures. Mater Horiz 2017;4:673–80. https://doi.org/10.1039/C7MH00129K.
[7] Jiménez N, Romero-García V, Pagneux V, Groby J-P. Rainbow-trapping absorbers: broadband, perfect and asymmetric sound absorption by subwavelength panels for transmission problems. Sci Rep 2017;7:13595. https://doi.org/10.1038/s41598-017-13706-4.
[8] Jiménez N, Groby JP, Pagneux V, Romero-García V. Iridescent perfect absorption in critically-coupled acoustic metamaterials using the transfer matrix method. Appl Sci 2017;7:618. https://doi.org/10.3390/app7060618.
[9] Garza-Agudelo DM, Cutanda Henriquez V, Jeong CH, Andersen PR. Characterization and optimization of the angle dependent acoustic absorption of 2D infinite periodic surfaces of Helmholtz resonators. J Theor Comput Acoust 2023;31. https://doi.org/10.1142/S2591728522500104.
[10] Almeida G do N, Vergara EF, Barbosa LR, Lenzi A, Mareze PH, et al. Acoustic analysis of a metasurface for normal and random incidence sound waves. Phys Lett Sect A, Gen At Solid State Phys 2022;451:128417. https://doi.org/10.1016/j.physleta.2022.128417.
[11] Climente A, Torrent D, Sánchez-Dehesa J. Sound focusing by gradient index sonic lenses. Appl Phys Lett 2010;97:104103. https://doi.org/10.1063/1.3488349.
[12] Lin S-CS, Huang TJ, Sun J-H, Wu T-T. Gradient-index phononic crystals. Phys Rev B 2009;79:094302. https://doi.org/10.1103/PhysRevB.79.094302.
[13] Torrent D, Sánchez-Dehesa J. Acoustic cloaking in two dimensions: a feasible approach. New J Phys 2008;10:063015. https://doi.org/10.1088/1367-2630/10/6/063015.
[14] Guild MD, García-Chocano VM, Kan W, Sánchez-Dehesa J. Acoustic metamaterial absorbers based on multilayered sonic crystals. J Appl Phys 2015;117:114902. https://doi.org/10.1063/1.4915346.
[15] Elliott AS, Venegas R, Groby JP, Umnova O. Omnidirectional acoustic absorber with a porous core and a metamaterial matching layer. J Appl Phys 2014;115:204902. https://doi.org/10.1063/1.4876119.
[16] Climente A, Torrent D, Sánchez-Dehesa J. Omnidirectional broadband acoustic absorber based on metamaterials. Appl Phys Lett 2012;100:144103. https://doi.org/10.1063/1.3701611.
[17] Henríquez VC, Sánchez-Dehesa J. Viscothermal effects in a two-dimensional acoustic black hole: a boundary element approach. Phys Rev Appl 2021;15:064057. https://doi.org/10.1103/PhysRevApplied.15.064057.
[18] Cavalieri T, Boulvert J, Gabard G, Romero-García V, Escouflaire M, Regnard J, et al. Graded and anisotropic porous materials for broadband and angular maximal acoustic absorption. Materials 2020;13. https://doi.org/10.3390/ma13204605.
[19] Torrent D, Håkansson A, Cervera F, Sánchez-Dehesa J. Homogenization of two-dimensional clusters of rigid rods in air. Phys Rev Lett 2006;96:204302. https://doi.org/10.1103/PhysRevLett.96.204302.
[20] Torrent D, Sánchez-Dehesa J. Anisotropic mass density by two-dimensional acoustic metamaterials. New J Phys 2008;10:023004. https://doi.org/10.1088/1367-2630/10/2/023004.

[21] Krokhin AA, Arriaga J, Gumen LN. Speed of sound in periodic elastic composites. Phys Rev Lett 2003;91:264302/1. https://doi.org/10.1103/PhysRevLett.91.264302.
[22] Gumen LN, Arriaga J, Krokhin AA. Metafluid with anisotropic dynamic mass. Low Temp Phys 2012;37:975–8. https://doi.org/10.1063/1.3672821.
[23] Ibarias M, Zubov Y, Arriaga J, Krokhin AA. Phononic crystal as a homogeneous viscous metamaterial. Phys Rev Res 2020;2:022053. https://doi.org/10.1103/PhysRevResearch.2.022053.
[24] Brunskog J, Glebe D, Garza-Agudelo D, Nilsson E. Absorption and scattering by perforated facings with periodic narrow slits. J Acoust Soc Am 2022;151:1847–59. https://doi.org/10.1121/10.0009826.
[25] Mechel FP. Sound fields at periodic absorbers. J Sound Vib 1990;136:379–412. https://doi.org/10.1016/0022-460X(90)90452-6.
[26] Allard JF, Atalla N. Propagation of sound in porous media: modelling sound absorbing materials. John Wiley and Sons; 2009.
[27] Verdière K, Panneton R, Elkoun S, Dupont T, Leclaire P. Transfer matrix method applied to the parallel assembly of sound absorbing materials. J Acoust Soc Am 2013;134:4648–58. https://doi.org/10.1121/1.4824839.
[28] Stinson MR. The propagation of plane sound waves in narrow and wide circular tubes, and generalization to uniform tubes of arbitrary cross-sectional shape. J Acoust Soc Am 1991;89:550–8. https://doi.org/10.1121/1.400379.
[29] Smits JMA, Kosten CW. Sound absorption by slit resonators. Acustica 1951;1:114–22.
[30] Morse P, Ingard K. Theoretical acoustics. McGraw-Hill; 1968.
[31] Cremer L, Müller HA. Principles and applications of room acoustics, vol. 2. London: Applied Science Publisher; 1982.
[32] Nijhof M. Viscothermal wave propagation. Ph.D. thesis. Netherlands: University of Twente; 2010.
[33] Berggren M, Bernland A, Noreland D. Acoustic boundary layers as boundary conditions. J Comput Phys 2018;371:633–50. https://doi.org/10.1016/j.jcp.2018.06.005.
[34] Andersen PR, Cutanda Henriquez V, Godinho L, Chazot J-D, Carbajo San Martín J. Characterization of acoustic metasurface absorbers using numerical methods including viscous and thermal losses. In: Proceedings of internoise 2019; 2019.
[35] Andersen PR, Cutanda Henriquez V, Aage N. On the validity of numerical models for viscothermal losses in structural optimization for micro-acoustics. J Sound Vib 2022;547:117455. https://doi.org/10.1016/j.jsv.2022.117455.
[36] MATLAB®. V. 9.9.0.1592791 (R2020b) update 5. Natick, Massachusetts: The MathWorks Inc.; 2020.
[37] Nocedal J, Wright SJ. Numerical optimization. New York: Springer; 2006.
[38] Andersen PR, Cutanda Henríquez V, Aage N. Shape optimization of micro-acoustic devices including viscous and thermal losses. J Sound Vib 2019;447:120–36. https://doi.org/10.1016/j.jsv.2019.01.047.
[39] Ryoo H, Jeon W. Perfect sound absorption of ultra-thin metasurface based on hybrid resonance and space-coiling. Appl Phys Lett 2018;113:121903. https://doi.org/10.1063/1.5049696.
[40] Garza-Agudelo DM. Acoustic absorbing metamaterials for multidirectional incident waves. Ph.D. thesis. Denmark: Technical University of Denmark; 2022. Available at https://orbit.dtu.dk/en/publications/acoustic-absorbing-metamaterials-for-multidirectional-incident-wa.
[41] Li Y, Assouar BM. Acoustic metasurface-based perfect absorber with deep subwavelength thickness. Appl Phys Lett 2016;108:063502. https://doi.org/10.1063/1.4941338.
[42] Wang X, Zhou Y, Sang J, Zhu W. A generalized model for space-coiling resonators. Appl Acoust 2020;158:107045. https://doi.org/10.1016/j.apacoust.2019.107045.
[43] Guo J, Fang Y, Jiang Z, Zhang X. Acoustic characterizations of Helmholtz resonators with extended necks and their checkerboard combination for sound absorption. J Phys D, Appl Phys 2020;53:505504. https://doi.org/10.1088/1361-6463/abb5d8.
[44] Ji J, Li D, Li Y, Jing Y, Jing Y. Low-frequency broadband acoustic metasurface absorbing panels. Front Mech Eng 2020;6:1–13. https://doi.org/10.3389/fmech.2020.586249.
[45] Vergara EF, Almeida GN, Barbosa LR, Lenzi A, Carvalho De Sousa A. Broadband and low-frequency sound absorption of modified Helmholtz resonator combined with porous layer addition. J Appl Phys 2022;132:135114. https://doi.org/10.1063/5.0108807.
[46] ISO 10534-2. Determination of sound absorption coefficient and impedance in impedance tubes. Part 2: transfer-function method 1998.
[47] Zieliński TG, Opiela KC, Pawłowski P, Dauchez N, Boutin T, Kennedy J, et al. Reproducibility of sound-absorbing periodic porous materials using additive manufacturing technologies: round robin study. Addit Manuf 2020;36:101564. https://doi.org/10.1016/j.addma.2020.101564.
[48] Kennedy J, Flanagan L, Dowling L, Bennett GJ, Rice H, Trimble D. The influence of additive manufacturing processes on the performance of a periodic acoustic metamaterial. Int J Polym Sci 2019;2019:7029143. https://doi.org/10.1155/2019/7029143.